Geometrical influence on vortex shedding in turbulent axisymmetric wakes

J. Nedić,[1, a)] O. Supponen,[1] B. Ganapathisubramani,[2] and J. C. Vassilicos[1, b)]

[1)] *Turbulence, Mixing and Flow Control Group, Department of Aeronautics, Imperial College London, London SW7 2AZ, UK*

[2)] *Aerodynamics and Flight Mechanics Research Group, University of Southampton, Southampton SO17 1BJ, United Kingdom*

(Dated: 23 February 2015)

We investigate the structures generated by the vortex shedding mechanism in turbulent axisymmetric wakes of non-axisymmetric plates, including a square plate and a series of fractal plates, and compare the results to a disk. For a given characteristic length ℓ, all plates have the same frontal area A, since $\ell = A^{0.5}$, but the length of the perimeter, and the irregularity of the perimeter, were varied in a fractal manner thus allowing us to investigate the effect of boundary conditions. Measurements were taken over a large range of downstream and radial distances in order to obtain a more robust measure for the vortex shedding energy. It was found that the fractal plates are able to reduce the vortex shedding energy by as much as 60% compared to the disk and square plates. It was also found that the frequency at which the vortex shedding structures are generated and the manner in which they organise themselves in the wake are independent of the boundary conditions of the wake generator. The results suggest that the main function of the multi-scale segments around the perimeter of the plates are to re-distribute the energy to a broader range of scales in the flow, which could explain the previously observed increase in drag coefficient for the fractal edged plates.

[a)]jnedic@uottawa.ca. Present address: Department of Mechanical Engineering, University of Ottawa, Ottawa, ON, Canada K1N 6N5

[b)]j.c.vassilicos@imperial.ac.uk

I. INTRODUCTION

Turbulent shear flows such as boundary layers, jets, wakes and mixing layers, are known to contain organised, or coherent, large-scale structures[1] which account for up to 20-25% of the total energy of the flow[2]. It has recently been shown, for example, that using a model based on these structures alone, one is able to obtain first and second order statistics (i.e. mean flow and Reynolds stress profiles) of turbulent axisymmetric jets and wakes[3]. For a bluff body, one such example of a large-scale coherent structure are those created by the vortex shedding mechanism.

For two-dimensional wakes, the large-scale structures associated with the vortex shedding mechanism have a significant contribution to the drag force of bluff bodies, as well as the acoustic noise. It has been argued that coherent structures are the most amenable to external flow control[2] and as such, they have featured heavily in flow control strategies where numerous passive and active flow control methods have shown that by breaking the two-dimensional nature of these structures, one is able to reduce the vortex shedding energy as well as the mean and fluctuating drag - see, for example, Choi, Jeon & Kim[4]. The relationship between the drag force and the vortex shedding mechanism for three-dimensional bodies is not yet fully understood. Understanding these structures and the role they play is therefore of vital importance if we are to expand, amongst other things, our basic understanding of turbulent shear flows and optimisation of flow control strategies for such flows.

Of the various turbulent shear flows listed above, our understanding of the large-scale coherent structures in turbulent axisymmetric wakes is comparatively sparse. Johansson and George[5] provide a extensive review of the various qualitative and quantitative studies that have investigated the structure of turbulent axisymmetric wakes. Of particular interest in the context of this study are the works by Roberts[6], Fuchs et al[7], Berger et al[8], Cannon[9], Lee and Bearman[10], Cannon et al[11] and Johansson et al[12]. This body of work investigated the large-scale coherent structures in axisymmetric wakes through means of cross-correlations of multiple points in space. By decomposing these signals, either through azimuthal Fourier decomposition or proper orthogonal decomposition (POD), it was possible to determine the most energetic modes within the wake.

It is generally accepted, and several stability analysis have shown e.g. Monkewitz[13], that

the frequency associated with the vortex shedding is the most dominant energetically and is associated with the first azimuthal mode, i.e. $m = 1$, in the decomposition. Several experiments have also shown a second azimuthal mode ($m = 2$), to exist with a near zero frequency, however there has been debate as to the physical meaning of this particular feature. Roberts[6] attributed this frequency to the "slow, random variation in the orientation" of the vortex shedding motion. This was dismissed by Fuchs et al[7], where through azimuthal decomposition they determined that these two frequencies had different azimuthal mode numbers and were therefore two distinct large-scale features of the wake. Johansson, George and Woodward[12], as well as a later study by Johansson and George[5] used the slice-POD method to investigate the structure of the wake and argue that the second mode is linked to a 'temporal variation of the wake' whereby the mean flow would twist independently from the helical motion of the vortex shedding. As with previous studies, they found the $m = 1$ azimuthal mode to be the most energetic, but was decaying rapidly.

For the most part, the large-scale coherent structures in turbulent axisymmetric wakes have been generated by axisymmetric bodies, with the study by Higuchi et al[14], who investigated the large-scale structures behind a series of regular polygon plates using flow visualisation techniques, being a notable exception. In a recent study by Nedić, Ganapathisubramani & Vassilicos[15], turbulent axisymmetric wakes were generated by a series of flat plates with irregular perimeters. These fractal plates had the same frontal area with varying fractal dimensions D_f and iterations n, where a higher D_f is characterised as a 'rougher' pattern whilst a higher n corresponds to an increase in the perimeter for a given D_f. As either of these parameters increases, the drag coefficient of the plates increases up to a threshold value beyond which it suddenly drops. It was shown that the Strouhal number of the vortex shedding was universal if the characteristic length of the plate was used i.e. $St_{vs} = (f_v \ell)/U_\infty = 0.11 \pm 0.005$, where f_v is the frequency of the vortex shedding, $\ell = \sqrt{A}$ is the characteristic length with A being the frontal area of the plate. Based on a single radial and downstream position, the authors showed that the intensity of the vortex shedding would reduce with increasing D_f and n. This finding should be taken with some caution as the wakes of the fractal plates are smaller than the equivalent disk and square; in fact they are found to grow at a different rate to the disk and square[16], hence the measurements may have been taken at two different relative radial positions in the wake.

The aim of this study is two-fold; firstly there is a need to comprehensively examine

the vortex shedding feature of these fractal plates by taking into account measurements from several radial and downstream positions. Secondly, since the majority of studies have used axisymmetric bodies to generate the wake and hence the coherent structures, do the complexity and particular symmetries of fractal plates i.e. the boundary conditions, change these coherent structures? Specifically, is the vortex shedding mechanism still a dominant feature of the flow?

II. EXPERIMENTAL SET-UP

A. Plate specifications and suspension

To generate the turbulent axisymmetric wakes, we use the fractal plates described in Nedić et al[16], all of which have been shown to generate a statistically axisymmetric mean wake within a few characteristic lengths downstream of the plate. Three parameters can be used to define the plates; fractal dimension (D_f), fractal iteration (n) and the characteristic length ($\ell = \sqrt{A}$). We use a series of plates with fractal dimensions $D_f = 4/3$ and $D_f = 1.5$, as well as three sets of characteristic lengths $\ell = 128mm, 64mm$ and $50mm$, giving a Reynolds number based on the characteristic length of $Re_\ell \approx 82,000$ for the $\ell = 128mm$ plate and $Re_\ell \approx 41,000$ for the $\ell = 64mm$ and $\ell = 50mm$ plates. The plates and their properties can be found in figure 1 and table I. All plates were mounted on a small aluminium mount of dimension 20mm x 20mm x 6mm, which was suspended in the middle of the tunnel, 0.5m from the start of the test-section, using four 0.2mm piano wires. For wind speeds less than $U_\infty = 15ms^{-1}$, there was no significant vibration of the plates.

B. Single-point measurements

A closed recirculating loop wind tunnel, with a 9:1 contraction ratio, a working cross-section of 0.91m x 0.91m and a working length of 4.25m was used for the single point measurements. The freestream velocity was set to $U_\infty = 10ms^{-1}$ for all plates except the $\ell = 50mm$ plates, for which $U_\infty = 12.8ms^{-1}$(The background turbulence level was about 0.05% for all cases). The tunnel free-stream velocity was controlled and stabilised with a PID feedback system using the static pressure difference across the 9:1 contraction and the temperature inside the test section measured half way along it. Both the pressure and the

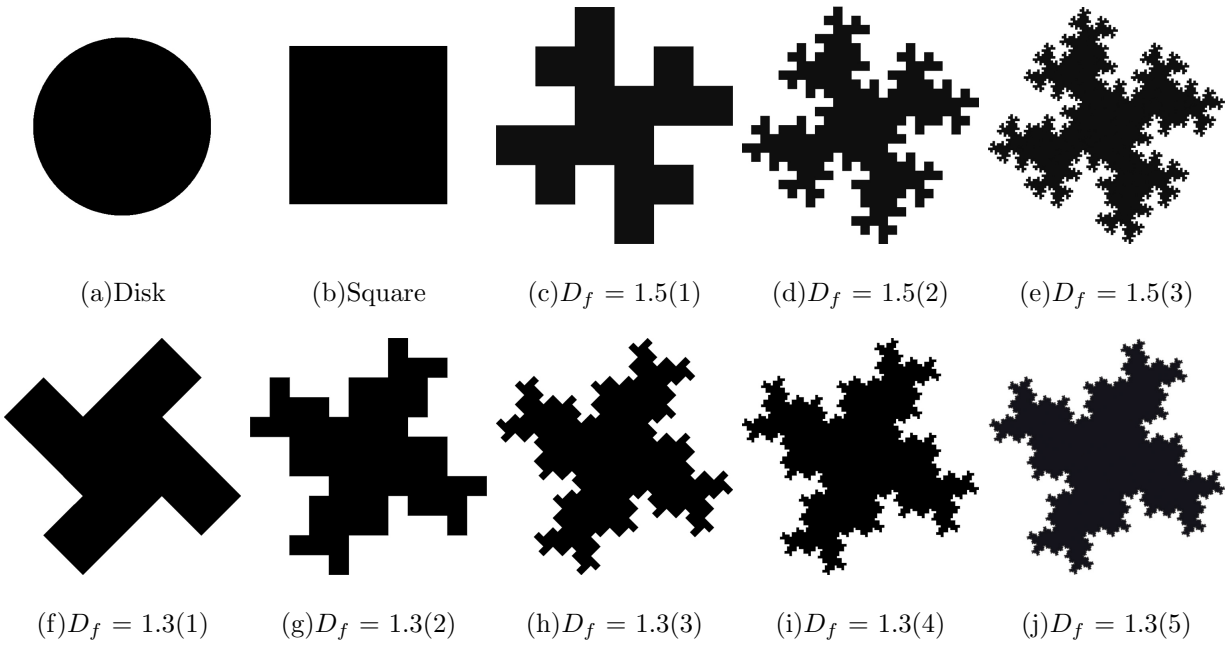

FIG. 1: Scaled drawings of flat plates used in this experiment

temperature were recorded with a Furness Controls Micromanometer FCO510 which also had an atmospheric gauge sensor attached to give instantaneous air density readings.

Hot-wire anemometry measurements were taken downstream of the wake generators using a Dantec Dynamics 55P51 X-wire, driven by a Dantec StreamLine CTA system. The Pt-W wires were 5μm in diameter, 3mm long with a sensing length of 1.25mm and connected to a 55H24 6mm probe holder. Measurements were taken at downstream distances of x = 5ℓ to 50ℓ in 5ℓ intervals for the ℓ = 64mm plates, and up to x = 25ℓ for the ℓ = 128mm plates. To obtain mean turbulent wake profiles, the probe was traversed in 15mm vertical intervals normal to the streamwise x-axis, covering a distance of 390mm from the centre-line. For the smaller plates with ℓ = 64mm at the two closest distances x/ℓ = 5 and 10, the X-wire was traversed in 10mm steps up to a distance of 260mm from the centre-line as these particular wake widths were considerably smaller and more data points were required to get good spatial resolution. Data was sampled using a 16-bit National Instruments NI-6229 (USB) data acquisition card, at a rate of 20kHz for 30 seconds, which was sufficient to obtain converged statistics of the mean and fluctuating velocities for both velocity components. The measurement uncertainty, using a 95% confidence interval, along the streamwise axis is estimated to be less than 1% of the measured value for the mean flow and less than 6% of

Name	D_f	n	P_n/ℓ	$l_n(mm)$			Symbol
				ℓ = 128mm	ℓ = 64mm	ℓ = 50mm	
				t = 2.5mm	t = 1.25mm	t = 1.25mm	
Disk	1.0	0	$2\sqrt{\pi}$	-	72.22	56.42	●
Square	1.0	0	4	128.00	64.00	50.00	■
D_f = 1.3(1)	4/3	1	5.64	45.25	-	17.68	△
D_f = 1.3(2)	4/3	2	8.00	16.00	-	6.25	▷
D_f = 1.3(3)	4/3	3	11.32	5.66	-	2.21	▽
D_f = 1.3(4)	4/3	4	16.00	2.00	1.00	0.78	◁
D_f = 1.3(5)	4/3	5	22.64	0.71	-	-	◇
D_f = 1.5(1)	3/2	1	8.00	32.00	16.00	12.5	▲
D_f = 1.5(2)	3/2	2	16.00	8.00	4.00	3.12	▶
D_f = 1.5(3)	3/2	3	32.00	2.00	1.00	0.78	▼

TABLE I: Fractal plate dimensions - D_f is the fractal dimension, n is the iteration of the fractal pattern, P_n is the perimeter, t is the thickness of the plate and l_n is the length of each segment at the given iteration in mm, where for the disk, this value is the diameter of the plate.

the measured value for $\langle u'^2 \rangle$ and $\langle v'^2 \rangle$.

C. Two-point measurements

For the two-point measurements, data was sampled in the same wind tunnel using two Dantec Dynamics 55P16 single wires, one of which was fixed in space and the second attached to a stepper motor that acquired data between $0° \leq \varphi \leq 180°$ at the same distance from the centreline. The two wires were driven by a Dantec Dynamics Streamline CTA, with data

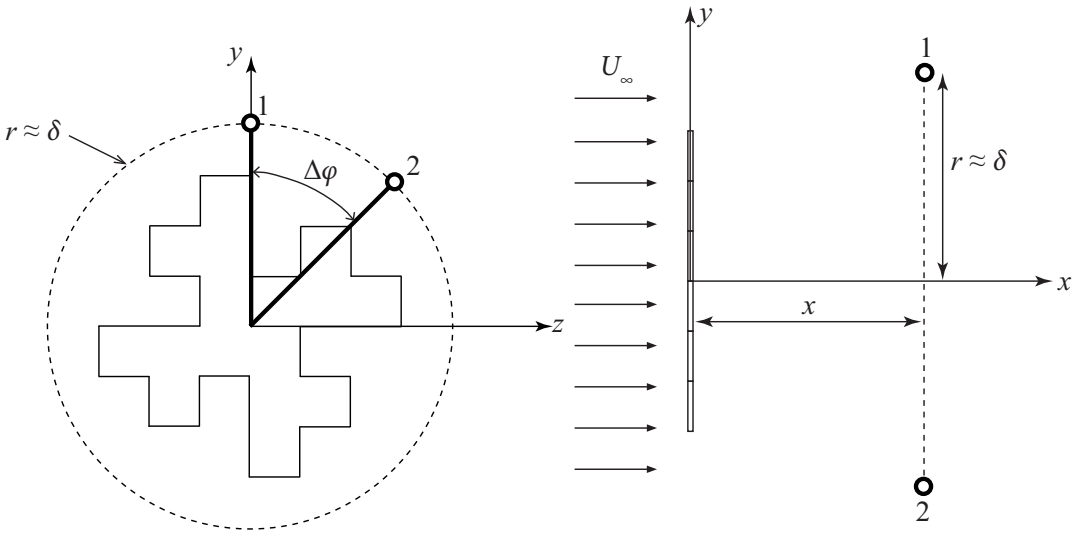

(a)Head-on view (b)Side view

FIG. 2: Cross-sectional view of the experimental setup and coordinate system for two-point measurements. Note that the hot-wire probes are placed at positions '1', which is a fixed position for all measurements at a given downstream location, and '2' which varies with some azimuthal separation of $\Delta\varphi$

sampled at 1kHz for 300 seconds. Measurements were taken for downstream distances of $x = 5\ell, 10\ell$ and 20ℓ, with the radial position for each of the downstream distances set such that $r \approx \delta$, where δ is the integral width of the wake and defined as $u_0\delta^2 = \int_0^\infty (U_\infty - U) r dr$; here u_0 is the velocity deficit at the centre of the wake and U is the mean streamwise velocity. This particular radial distance was chosen as it coincides with the position where the vortex shedding energy is at its strongest, as will be shown in section III.

III. DOWNSTREAM EVOLUTION OF LARGE-SCALE STRUCTURES

In Nedić et al.[15], it was claimed that the vortex shedding energy for the fractal plates was nearly four times smaller compared to the square plate; however, this finding is based on measurements at a single downstream and radial position. Although the wakes of these fractal plates are growing at a faster rate, they are, in the downstream distances considered here, smaller than the disk and the square plate[16]. Hence attempting to determine the reduction in the intensity of the vortex shedding at a single radial position may be misleading,

or at the very least incomplete.

In figure 3 we show a pre-multiplied energy spectrogram for three $\ell = 128mm$ plates at downstream distances of $x = 10\ell$ and $x = 20\ell$. A dominant peak is identified in these plots for a Strouhal number of $St = 0.11 \pm 0.005$, which is in good agreement with previous measurements. Although only a single downstream position and a selection of plates are shown, it should be noted that a peak was observed for the same Strouhal number for all downstream positions and plates. A further observation can also be made from figure 3 in that the position of the peak moves to higher r/ℓ as x/ℓ increases. It is worth noting that the Strouhal number at which the vortex shedding occurs (St_{vs}) is also found to be $St_{vs} = 0.11$ for the disk, and if the diameter of the disk was used instead of the characteristic length, then one would recover the same vortex shedding Strouhal number found in the literature i.e. $St^{*}_{vs} = 0.13$.

Knowing the frequency at which the vortex shedding occurs, we expand our analysis with a more robust measure for the intensity of the vortex shedding itself, by taking into account both the streamwise and radial velocity components for a range of radial and downstream distances. Typical energy spectra, at a single downstream and radial position, is shown in figure 4 for the square plate and the $D_f = 1.5(3)$ which, as will be shown later, produced the largest reduction in the vortex shedding energy. This figure now presents an aspect of the vortex shedding that needs to be addressed: is the vortex shedding energy defined at a single frequency or over a range of frequencies? If the spectra are integrated over too narrow a frequency band, then we may not adequately represent the change in vortex shedding energy - see figure 4(a) for example. As we increase the frequency bandwidth, i.e. from figure 4(a) to 4(b) to 4(c) to 4(d), we may reach a point where we would effectively measure the energy of a range of large-scale structures, including the structures generated by the vortex shedding mechanism.

To address these issues, we begin by defining the vortex shedding energy E_{vs} as $E_{vs} = E_{vs1} + E_{vs2}$ where $E_{vs1} = \int_{f_1}^{f_2} E_{uu} df$ and $E_{vs2} = \int_{f_1}^{f_2} E_{vv} df$, and E_{uu} and E_{vv} are the energy spectra of the fluctuating streamwise and radial velocity components respectively, both normalised with the freestream velocity U_∞. Note that the freestream velocity is chosen to normalise the velocity data as it provides a better comparison for the effects of boundary conditions on the vortex shedding energy, since we compare plates with the same characteristic length and inflow velocity conditions. We define a bandwidth over which the energy

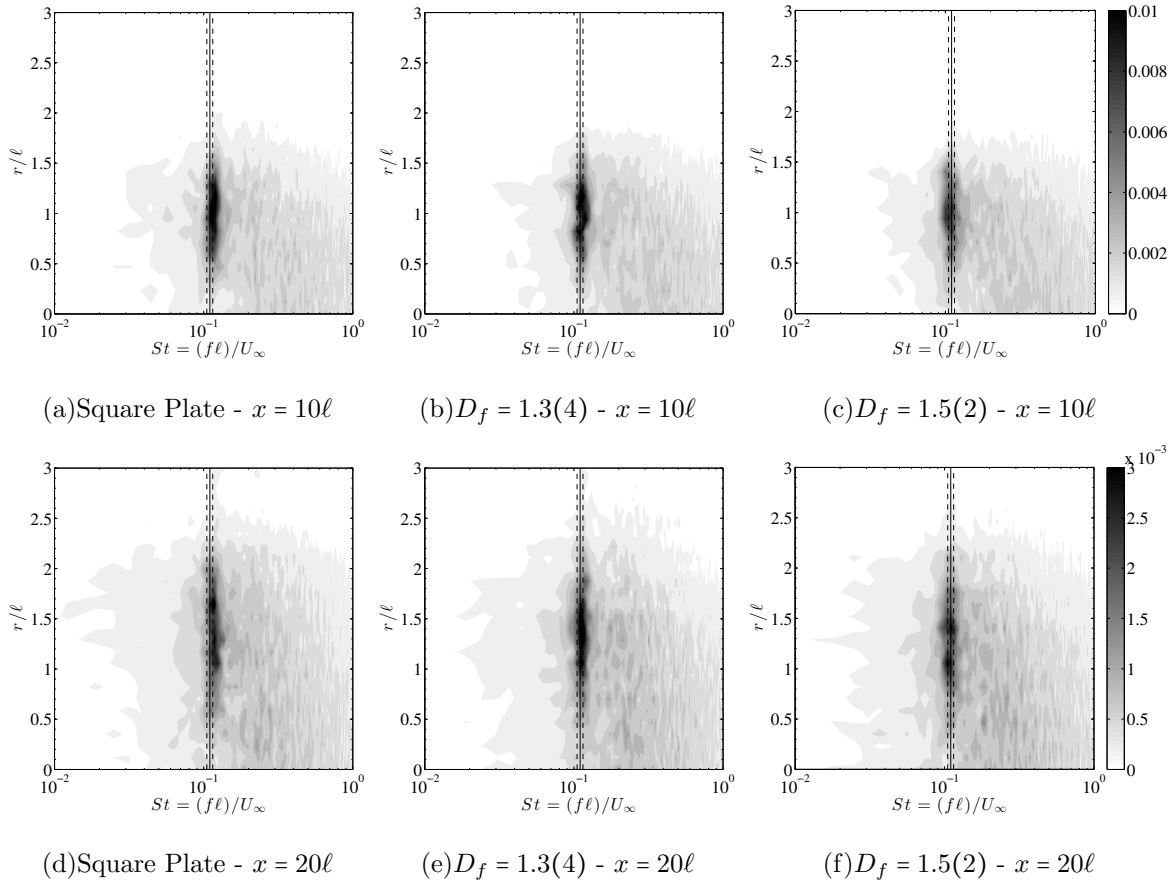

(a)Square Plate - $x = 10\ell$ (b)$D_f = 1.3(4)$ - $x = 10\ell$ (c)$D_f = 1.5(2)$ - $x = 10\ell$

(d)Square Plate - $x = 20\ell$ (e)$D_f = 1.3(4)$ - $x = 20\ell$ (f)$D_f = 1.5(2)$ - $x = 20\ell$

FIG. 3: Contour plots of energy spectra multiplied by the frequency f for all radial positions at $x = 20\ell$. The black line indicates the point where $St = 0.11$, with the dashed ones indicating ±0.005.

spectra are integrated as $\Delta f = f_2 - f_1$, where f_2 and f_1 are the upper and lower limits of the integral respectively and centre about the vortex shedding frequency $f_v = (0.11U_\infty)/\ell$ i.e. $St_{vs} = 0.11$ is the Strouhal number at which the vortex shedding occurs. This is a similar method to Rind and Castro[17]. Once a value of E_{vs} has been obtained, we can use equations 1 and 2 to obtain the energy in a given spatial domain with R being the last radial data point, which is the same for all plates at each downstream location, and where $X_1 = 5\ell$ and $X_2 = 25\ell$ for the $\ell = 128mm$ plates. It is important to keep in mind throughout the reading of this paper that the vortex shedding energy comprises contributions from both the vortex shedding and the turbulence at and around the vortex shedding frequency.

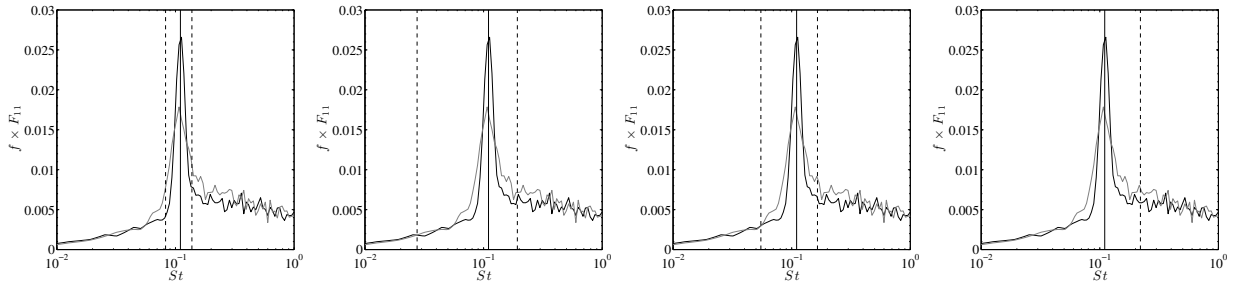

(a)$\Delta f/St_{vs} = 1/2$ (b)$\Delta f/St_{vs} = 1$ (c)$\Delta f/St_{vs} = 3/2$ (d)$\Delta f/St_{vs} = 2$

FIG. 4: Representative pre-multiplied energy spectra for the square plate (Black) and $D_f = 1.5(3)$ plate (Grey), showing various frequency integral limits. Solid vertical line indicates $St = 0.11$. Data collected at $x = 5\ell$ and $r = 50mm$ from the centre-line.

$$\xi(x) = \frac{2\pi}{\ell^2} \int_0^R E_{vs}(r) r dr \tag{1}$$

$$\Xi = \frac{1}{\ell} \int_{X_1}^{X_2} \xi(x) dx \tag{2}$$

From the above discussion, it is clear that the intensity of the vortex shedding in a given spatial domain, Ξ, ultimately depends upon the choice of Δf; hence Δf is an important factor and requires closer attention. In figure 5 we show the relative change in Ξ between the fractal plates and the square for a range of $\Delta f/St_{vs}$, noting that $\Delta f/St_{vs} = 0$ is the same as taking the energy of the spectra at f_v. This figure clearly shows the importance of $\Delta f/St_{vs}$. For example, the $D_f = 1.5(3)$ plate shows a 60% reduction in Ξ compared to the square plate for $\Delta f = 0$ (see figure 5(b)), whilst the reduction is closer to 25% when $\Delta f = 2St_{vs}$ (see figure 5(c)). Figures 5(b) and 5(c) also illustrate the effect both fractal dimension and iteration have on the change in Ξ, with this value decreasing compared to the square plate as both D_f and n increase.

Concluding that the fractal plates do decrease the vortex shedding energy compared to the square plate, and that this reduction is constant for $\Delta f/St_{vs} \geq 1$, we take the vortex shedding energy obtained with $\Delta f = St_{vs}$, deemed to be a fair compromise between minimising any possible influence from extremely large-scale structures as well as smaller scale structures at higher frequencies, and expand our analysis briefly to the $\ell = 64mm$ plates, for which measurements were taken over a larger range of downstream distances. These plates

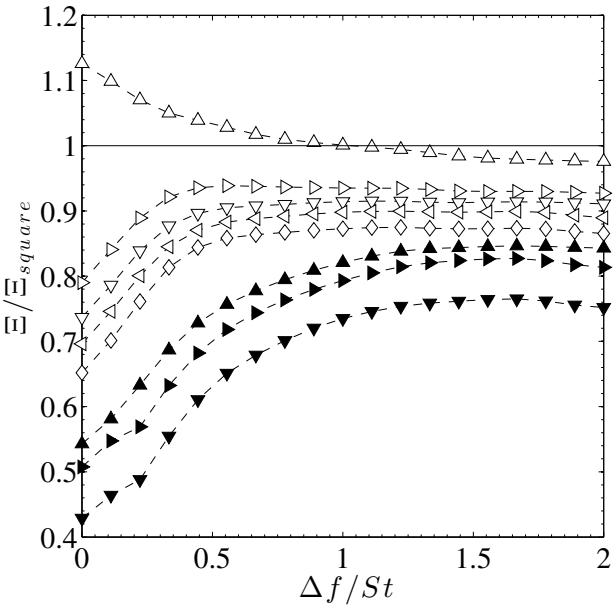

(a)Range of $\Delta f/St_{vs}$

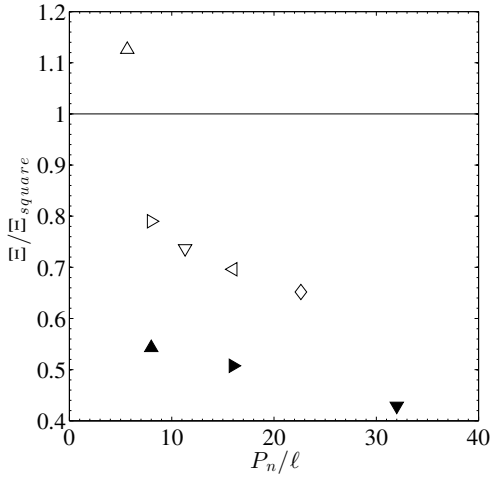

(b)$\Delta f = 0St_{vs}$

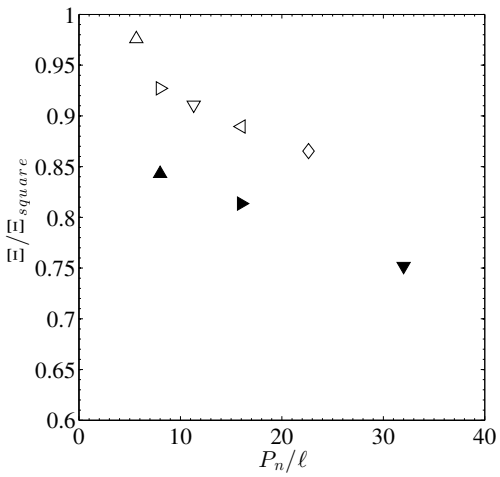

(c)$\Delta f = 2St_{vs}$

FIG. 5: Change in the vortex shedding energy relative to the square plate, see Table I for label definition.

therefore allow us to investigate more thoroughly the influence of the limits in equation 2, i.e. the choice of X_1 and X_2. With the $D_f = 1.5(3)$ showing the largest reduction in Ξ compared to the square plate - see figure 5 - we therefore present in figure 6 the ratio of Ξ between these two plates for various values of X_2, where in figure 6(a) we set $X_1 = 5\ell$ and $X_1 = 10\ell$ in 6(b). In this figure, we also show the results for $\Delta f = 0St_{vs}$ and $\Delta f = 2St_{vs}$. A clear drop in

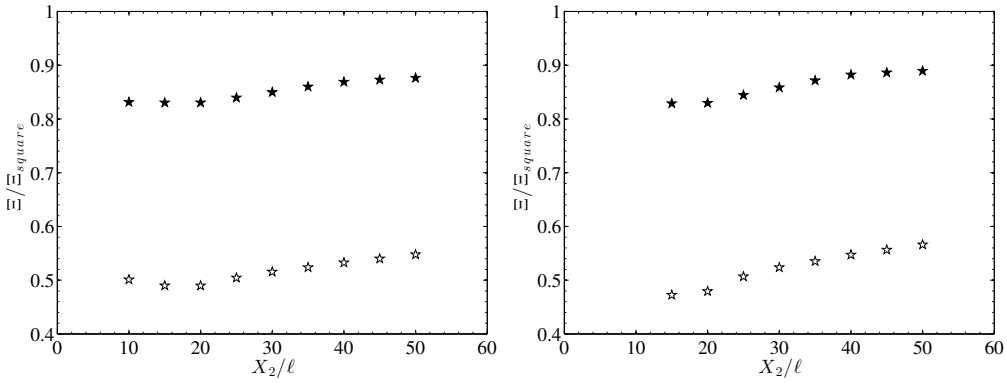

(a)$X_1 = 5\ell$ (b)$X_1 = 10\ell$

FIG. 6: Change in energy of vortex shedding for $D_f = 1.5(3)$ plate compared to the square plate, $\ell = 64mm$ for both plates, as a function of X_2 for $\Delta f = 0St_{vs}$ ($\star$) and $\Delta f = 2St_{vs}$ ($\star$)

the energy of the vortex-shedding is again observed between these two plates, whose characteristic length is now $\ell = 64mm$ and therefore the Reynolds number has halved. We note a small increase in the ratio as X_2 is increased, as well as no discernible difference between the two graphs in figure 6. It is therefore likely that any small amounts of asymmetry that may exist at $x = 5\ell$ are negligible in the analysis of the vortex shedding energy.

From this data, it is also possible to investigate how long it takes for the vortex shedding energy to subside to below, say, 5% of their original value, thus gaining a better idea of how far downstream these structures persist. This is shown in figure 7 where each sub-figure is scaled with the peak in intensity in that sub-figure and the contour levels are set to 5%, 10%, 20%, 40% and 80% of peak intensity. Although the intensity of the vortex shedding from the square plate is relatively large compared to the fractal plates, it quickly dissipates. By $x \approx 25\ell$ the intensity for the disk and square plate has already reached 5% and that there appears to be very little difference between the results of the square plate and the disk. Comparing this to the $D_f = 1.3(4)$ plate first, we note that the intensity of the vortex shedding at the centre-line reaches 5% of its peak value at $x \approx 30\ell$, whilst for the $D_f = 1.5(3)$ plate it is closer to $x \approx 40\ell$. Note that we find the same slow decay rate for the vortex shedding energy of the fractal plates, compared to the disk and square plate, with the vortex shedding energy calculated using a frequency bandwidth of $\Delta f = 0$ (i.e. at the vortex shedding frequency) and $\Delta f = 2St$.

The lack of any discernible difference in the wake of the disk and the square is surprising

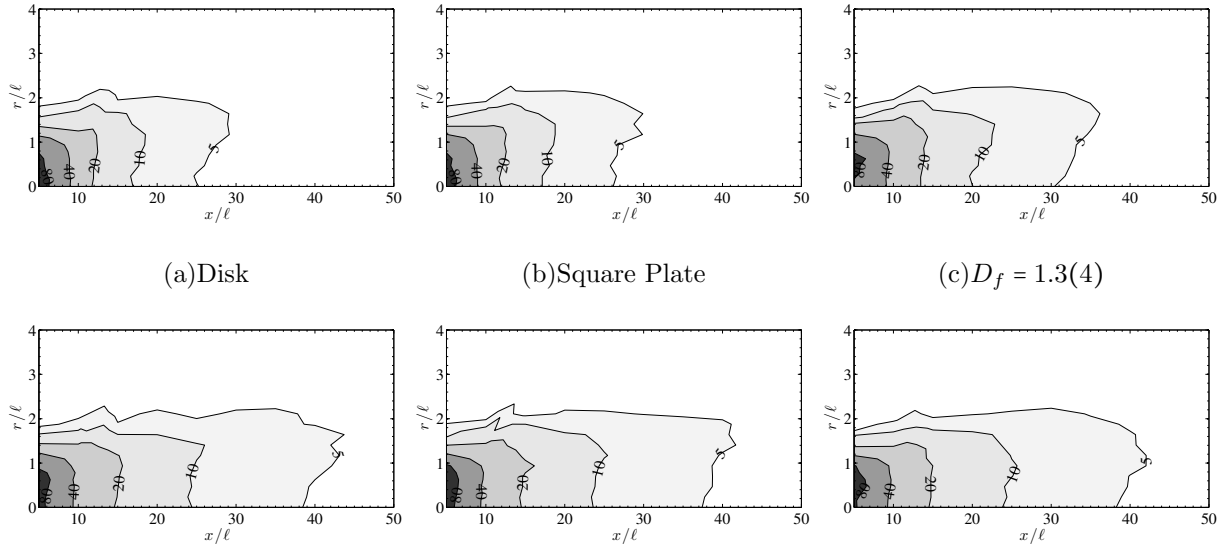

(a)Disk (b)Square Plate (c)D_f = 1.3(4)

(d)D_f = 1.5(1) (e)D_f = 1.5(2) (f)D_f = 1.5(3)

FIG. 7: Downstream evolution of the total vortex shedding energy E_{vs} obtained for $\Delta f = St_{vs}$, normalised by the maximum value in each sub-figure, across all downstream and radial positions. Contour levels are at 5%, 10%, 20%, 40% and 80% of peak intensity for each plate (all $\ell = 64mm$ plates).

since one would have expected the corners of the square plate to be a factor, but this does not appear to be the case at this Reynolds number and over the spatial extent investigated. Interestingly however, it appears that the 'global' length scale of the plate controls the frequency of the vortex shedding i.e. $\ell = \sqrt{A}$, whilst the smaller 'local' length scales around the perimeter of the plate influence the vortex shedding energy. By using fractal patterns it is possible to increase the number of these 'local' length scales whilst keeping the frontal area constant, and hence we find that as both fractal dimension and iteration increase, the energy of the vortex shedding decreases, as shown in figure 5. Although the vortex shedding energy for the fractal plates is lower compared to the disk and square plates, as much as 60% lower for $\Delta f/St_{vs} = 0$ (see figure 5), this energy decays slower as shown in figure 7, meaning either the shed vortices retain their energy for longer or the turbulence at these frequencies decays slower.

IV. THE STRUCTURE OF THE TURBULENT WAKE

Having addressed the first objective for this paper, as outlined at the end of Section I, we now turn our attention to the second. In the following section, we investigate the structure of the wake using Fourier decomposition on two-point measurements, similar to those done in the wake of a disk and other axisymmetric bodies[6–8,10,11].

A. Coherence and azimuthal Fourier decomposition

Following Fuchs et al[7], we analyse the large-scale structures by investigating two signals lying in the same plane parallel to the plate, say $u_1(t)$ and $u_2(t)$ where '1' denotes the time varying streamwise velocity signal from a probe at a fixed radial distance and '2' is the signal from the probe lying on the same circle about the centreline (same x and r), but with some azimuthal separation $\Delta\varphi$ - see figure 2. The cross-power spectral density of these signals is calculated and is such that:

$$E_{12}(f,\Delta\varphi) = C_{12}(f,\Delta\varphi) + iQ_{12}(f,\Delta\varphi) \tag{3}$$

where $C_{12}(f,\Delta\varphi)$ and $Q_{12}(f,\Delta\varphi)$ are known as the coincident and quadrature spectra respectively. Hence we note that the cross power-spectral density is complex, having a real ($\mathbb{R}$) and imaginary part ($\mathbb{I}$). From this data, the coherence function, γ_{12}, and the phase of the signal, θ_{12} can be obtained using equations 4 and 5, where $E_{11}(f)$ and $E_{22}(f)$ are the energy spectra of the fluctuating streamwise velocity at positions '1' and '2'.

$$\gamma_{12}(f,\Delta\varphi) = \frac{|E_{12}(f,\Delta\varphi)|}{(E_{11}(f)E_{22}(f))^{1/2}} \tag{4}$$

$$\theta_{12}(f,\Delta\varphi) = \arctan\left(\frac{Q_{12}(f,\Delta\varphi)}{C_{12}(f,\Delta\varphi)}\right) \tag{5}$$

Equation 4 will demonstrate the correlation of a particular large-scale structure i.e. at a particular f, with azimuthal separation. Fuchs et al[7] note that for an axisymmetric flow, the quadrature spectra $Q_{12}(f,\Delta\varphi)$ should be zero assuming no mean swirl is present in the flow, which we find to be the case for all of our plates, and so the phase angle will either be in phase or 180° out of phase. It is possible to decompose the data azimuthally and obtain the amount of fluctuating energy that resides in each mode, as shown in equation 6.

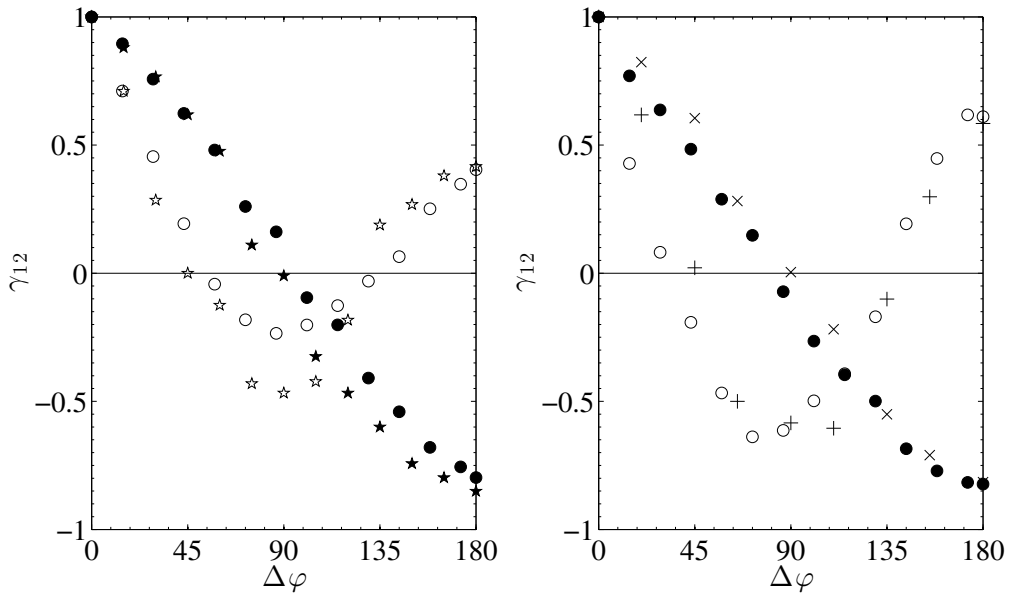

(a)$x = 5\ell$ (b)$x = 10\ell$

FIG. 8: Coherence coefficient γ_{12} for (a) disk at $x = 5\ell$ for $St = 0.004$ (○) and $St = 0.11$ (●), including corresponding Strouhal numbers (☆ | ★) from Lee & Bearman[10] at x = 3.84ℓ, and at $x = 10\ell$ in (b) where the data is compared to Roberts[6] at x = 9ℓ for $St^* \approx 0$ (+) and $St^* = 0.135$ (×)

$$C_{12,m}(f,m) = \frac{1}{\pi}\int_0^{\pi} C_{12}(f,\Delta\varphi)\cos(m\Delta\varphi)d(\Delta\varphi) \tag{6}$$

$C_{12,m}$ are therefore discrete coefficients of a Fourier series of C_{12}, as defined in equation 7. Note that with $\Delta\varphi = 0$, equation 7 is simply the sum of all the discrete coefficients of the Fourier series at a given frequency - $C(f) = \sum_{m=0}^{\infty} C_{12,m}(f,m)$ i.e. it is the total amount of fluctuating energy at a particular frequency. $C(f)$ can therefore be used to normalise equation 7 which will give us an indication of how important a particular mode is at a given frequency.

$$C_{12}(f,\Delta\varphi) = \sum_{m=0}^{\infty} C_{12,m}(f,m)\cos\left(m\Delta\varphi\right) \tag{7}$$

B. Comparison between a disk and square plate

As a validation of our data, we compare the coherence coefficient for the disk at a Strouhal number of $St = 0.11$ and at a near zero Strouhal number, taking the data at $St = 0.004$ as a representative test case, with the data from Roberts[6] and Lee & Bearman[10]. This is shown in figure 8, where we note good agreement with previous data, in particular with the data of Lee & Bearman[10] which was taken in the same wind tunnel.

We identify coherent structures in the wake by investigating the coherence coefficient across a range of frequencies, and selecting those frequencies, hence structures, where the coefficient is deemed to be sufficiently high. In figure 9, we show the coherence coefficient (left column), phase angle (centre column) and azimuthal decomposition (right column) for the disk and square plate. Note that for the coherence coefficient figures we have coloured any data for which there is less than 20% correlation i.e. $-0.2 \leq \gamma_{12} \leq 0.2$ as white to clearly identify the coherent structures in the wake. Note that for the coherence plots, solid lines are used to denote positive coherence values and dashed lines for negative values. Figure 9(a) clearly identifies two coherent structures, one at $St = 0.11$ and a second at a near zero Strouhal number, $St \approx 0$, and that these two frequencies coincide with the first two azimuthal modes as shown in figure 9(c). The phase angle plots, where the white regions are associated with those frequencies and azimuthal separations that have been discarded in the coherence plots, show the expected relation for the disk with the vortex shedding being out-of-phase at diametrically opposite sides of the plate.

In their comprehensive study, Fuchs et al[7] found that there was comparatively little difference in the structure of the wake generated by a disk and that of a 120° cone. However both of these bodies are axisymmetric and one could argue that there would not be a clear difference between them. The square plate on the other hand is not axisymmetric, although it has been shown to generate a statistically mean axisymmetric wake[16]. With its sharp corners, asymmetry and rotational symmetry, the spatiotemporal aspect of the structures within the wake could be different. From figure 9, this does not appear to be the case and we find that the square plate has the same coherent structures, phase angle and associated azimuthal wave numbers as the disk. The only noticeable difference is the slight reduction in the coherence coefficient, as can be seen in figure 9(a) and 9(d).

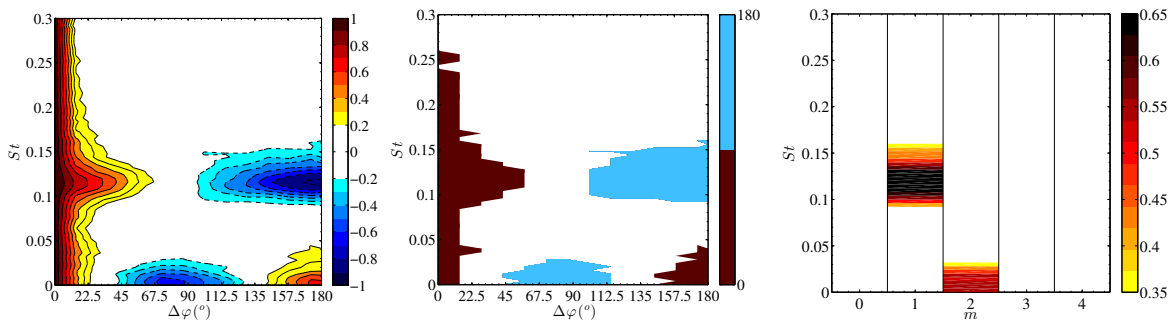

(a)γ_{12} - Disk (b)θ_{12} - Disk (c)$C_{12,m}/C$ - Disk

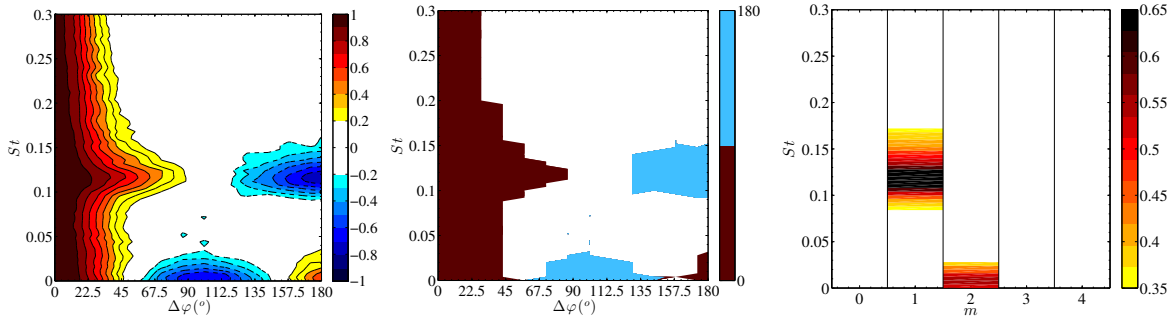

(d)γ_{12} - Square (e)θ_{12} - Square (f)$C_{12,m}/C$ - Square

FIG. 9: Coherence coefficient (γ_{12}), phase angle (θ_{12}) and normalised fluctuating energy per azimuthal mode ($C_{12,m}/C$) for the disk and the square plate at a downstream distance of $x = 10\ell$.

C. Wake structure of turbulent axisymmetric wakes from fractal plates

Figures 10 and 11 are similar to figure 9 and show the coherence coefficient (left column), phase angle (centre column) and azimuthal decomposition (right column) for the $D_f = 4/3$ and $D_f = 1.5$ families of plates respectively. Both families of fractal plates show a clear coherent structure at the vortex shedding frequency, however the coherence of this particular structure appears to be decreasing at larger azimuthal separations as both fractal dimension and iteration increase. In figure 12 we plot the coherence coefficient for this particular frequency for all the plates, which shows the reduction in coherence with increasing D_f and n more clearly. In figure 12(b), which shows the coherence coefficient at a downstream distance of $x = 10\ell$ and azimuthal separation of $\Delta\varphi = 180°$, the coherence coefficient decreases from 82% to 71% for the $D_f = 4/3$ series of plates and 70% to 52% for the $D_f = 1.5$ series of

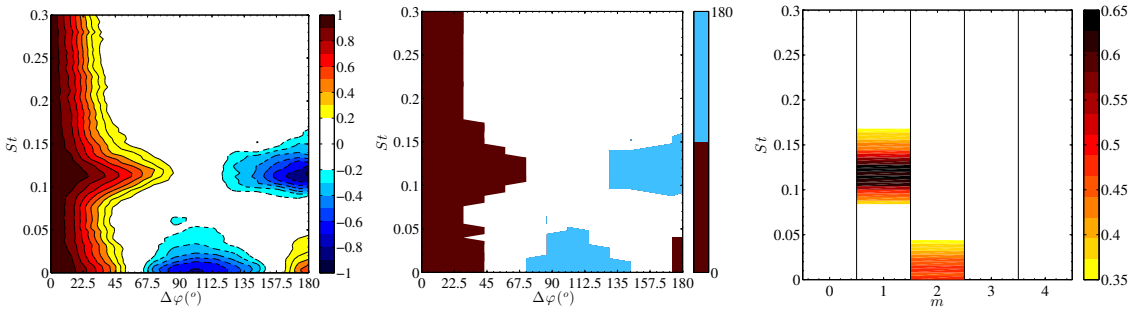

(a)$\gamma_{12} - D_f = 1.3(1)$ (b)$\theta_{12} - D_f = 1.3(1)$ (c)$C_{12,m}/C - D_f = 1.3(1)$

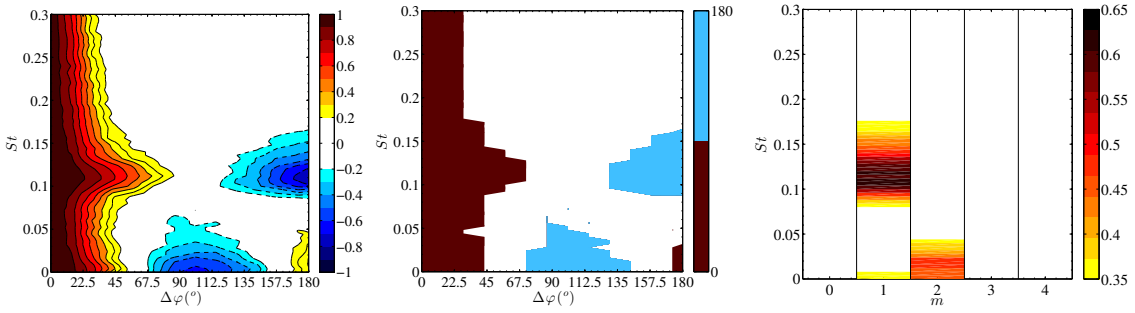

(d)$\gamma_{12} - D_f = 1.3(2)$ (e)$\theta_{12} - D_f = 1.3(2)$ (f)$C_{12,m}/C - D_f = 1.3(2)$

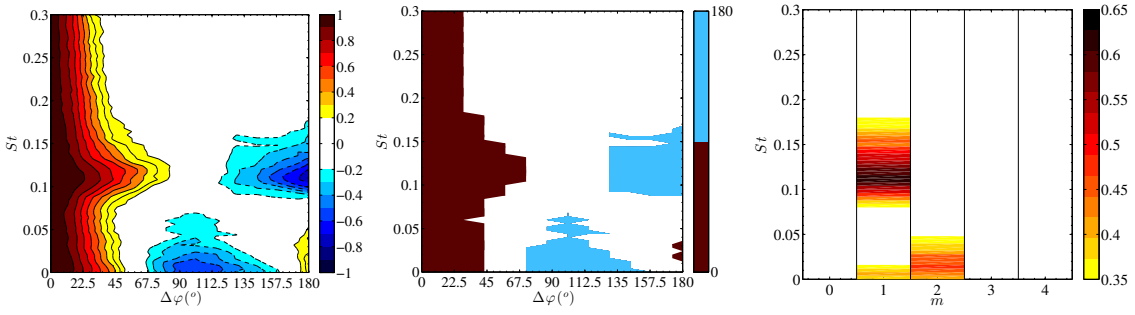

(g)$\gamma_{12} - D_f = 1.3(3)$ (h)$\theta_{12} - D_f = 1.3(3)$ (i)$C_{12,m}/C - D_f = 1.3(3)$

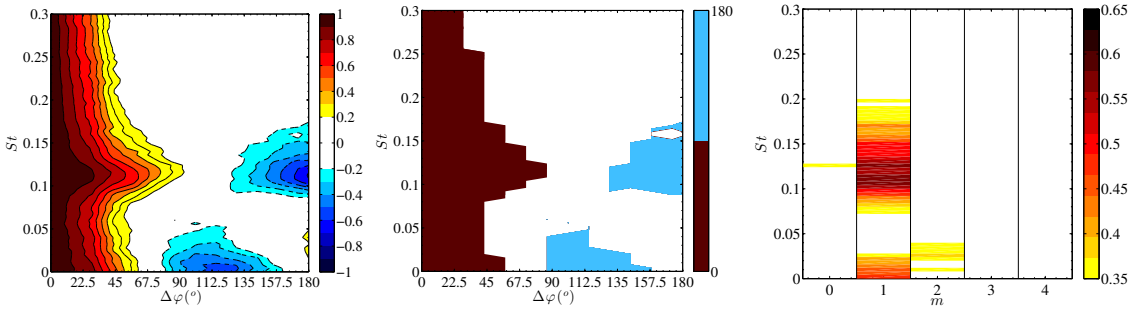

(j)$\gamma_{12} - D_f = 1.3(4)$ (k)$\theta_{12} - D_f = 1.3(4)$ (l)$C_{12,m}/C - D_f = 1.3(4)$

FIG. 10: Coherence coefficient (γ_{12}), phase angle (θ_{12}) and normalised fluctuating energy per azimuthal mode $(C_{12,m}/C)$ for the $D_f = 4/3$ family of plates, $x = 10\ell$

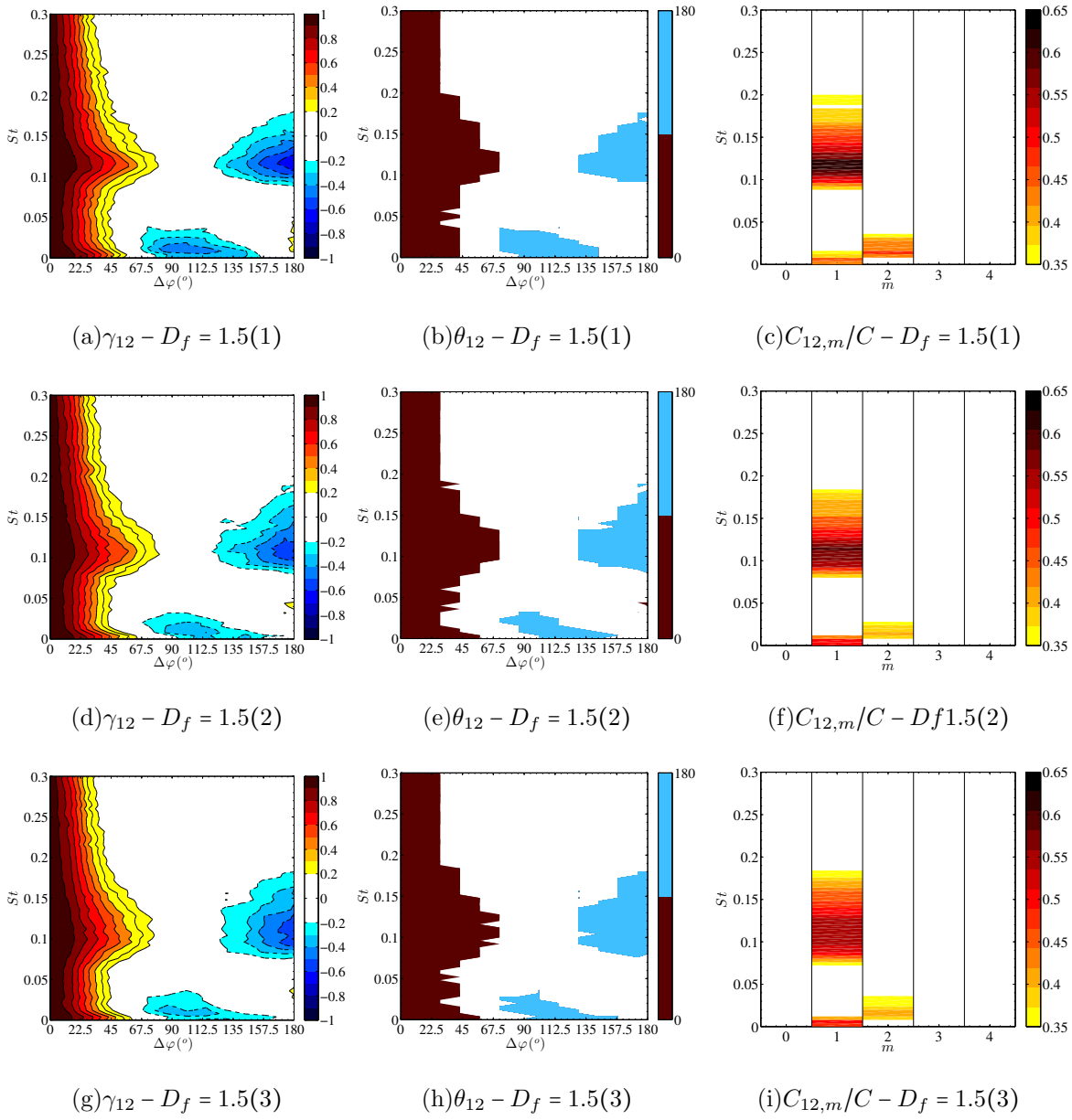

(a)$\gamma_{12} - D_f = 1.5(1)$ (b)$\theta_{12} - D_f = 1.5(1)$ (c)$C_{12,m}/C - D_f = 1.5(1)$

(d)$\gamma_{12} - D_f = 1.5(2)$ (e)$\theta_{12} - D_f = 1.5(2)$ (f)$C_{12,m}/C - Df1.5(2)$

(g)$\gamma_{12} - D_f = 1.5(3)$ (h)$\theta_{12} - D_f = 1.5(3)$ (i)$C_{12,m}/C - D_f = 1.5(3)$

FIG. 11: Coherence coefficient (γ_{12}), phase angle (θ_{12}) and normalised fluctuating energy per azimuthal mode ($C_{12,m}/C$) for the $D_f = 1.5$ family of plates, $x = 10\ell$

plates. Note also the reduction in coherence between the $D_f = 1.5(1)$ and $D_f = 1.3(2)$ plate, both of which have the same perimeter but a different fractal dimension, hence showing a clear effect of fractal dimension.

Focusing on this particular large-scale coherent structure, we note that just as it was for the disk and square plate, the phase of the signal is either in- or out-of-phase. Therefore

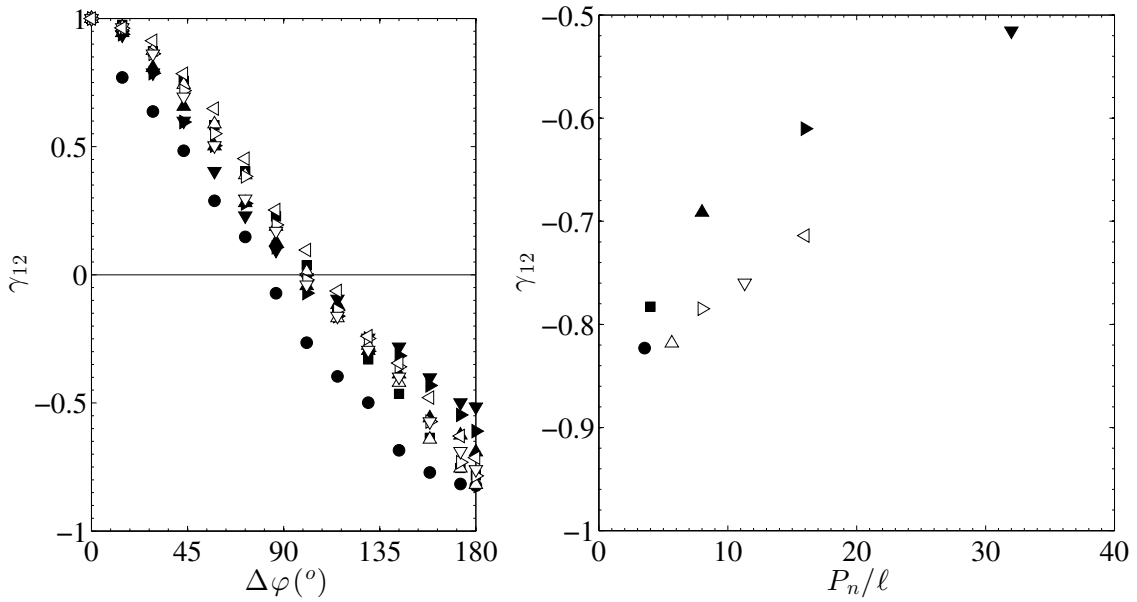

(a)For all $\Delta\varphi$ (b)$\Delta\varphi = 180°$

FIG. 12: Coherence coefficient γ_{12} at a Strouhal value of $St = 0.11$ for all the plates and a downstream distance of $x = 10\ell$ - see Table I for symbols

as well as the vortex shedding occurring at the same Strouhal number for all the plates, it would appear that the manner in which the vortices are shed is unchanged, that is to say that vortices are shed alternatively from diametrically opposite sides of the plate. This result is somewhat surprising; one would expect the chaotic nature of the plates to introduce an irregular spatial shedding mechanism. If measurements were to be taken immediately behind the plate, we would expect the vortex formation to follow the shape of the plate, as was shown in the flow visualisations of regular polygon plates by Higuchi et al.[14]. Soon after the initial formation period, Higuchi et al.[14] showed that their plates appeared to develop a ring-like vortical structure which would eventually break down into turbulence, a similar process found in the wake of a disk; however as the sharpness of the corners reduced, the position where this vortex ring would break down moved further downstream. For example, the structure behind the triangle would break up almost immediately whilst it was more persistent in the wake of an octagonal plate. Based on these findings, one might have expected the vortical structure of the fractal plates to be broken down more rapidly, yet as shown in figure 7, they appear to persist for longer. We even find that the vortex shedding

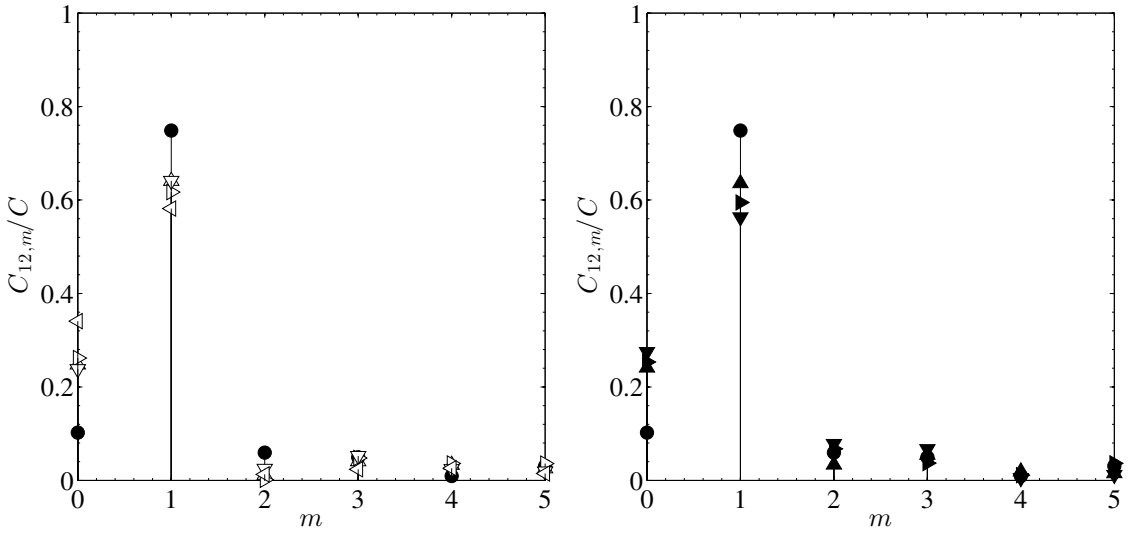

(a)D_f = 4/3 Plates (b)D_f = 3/2 Plates

FIG. 13: Normalised fluctuating energy per azimuthal mode number, $C_{12,m}/C$, at the vortex shedding Strouhal number St_{vs} = 0.11 for all fractal plates, taken at a downstream distance of x = 10ℓ. Data for the disk is shown as a comparison - see table I for symbols

frequency is still associated with azimuthal wave number m = 1, although as shown in figure 13, the amount of fluctuating energy contained in this mode, for this frequency, appears to diminish with increasing fractal iteration. For example we find that the relative amount of fluctuating energy ($C_{12,m}/C$) in mode m = 1 for the vortex shedding frequency is 73% for the disk at x = 10ℓ, whilst for the D_f = 1.5 series of plates it decreases from 63% to 55% with increasing fractal iteration. Therefore it appears that the vortex shedding is still a dominant feature of the wake and that it organises itself in much the same way as the flow in the wake of a disk.

The coherence plots in figures 10 and 11 also indicate a second coherent feature which, just as was the case for the disk and square plate, exists at very low frequencies. The results appear to suggest that the geometry of the plates may influence this structure. However, a detailed analysis of this feature requires additional data and is beyond the scope of the current study.

V. DISCUSSION

The overall objective of this study was to investigate the effects of physical boundary conditions (i.e. the geometry of the plate) on vortex shedding in turbulent axisymmetric wakes. This was achieved by keeping the frontal area of the wake generator and the inlet velocity constant, and varying the length and complexity of the perimeter of the plate i.e. by varying its fractal dimension and fractal iteration.

We have shown that the frequency at which the vortex shedding occurs is purely dependent upon the frontal area of the plates, no matter how irregular its perimeter may be. A more robust measure of the vortex shedding energy has also been presented and we find that not only does it systematically decrease with increasing fractal dimension and iteration, but the manner in which these structures are organised in the wake remains similar to those found in the wake of a disk. Hence it could be argued that just as the frequency at which the vortex shedding structures are generated is insensitive to the physical geometry of the wake generator, the manner in which they organise themselves in the wake is also insensitive to the physical geometry of the wake generator. Note that Monkewitz[13], whose linear parallel stability analysis of a family of axisymmetric wake profiles from axisymmetric bodies all yielded that the azimuthal mode $m = 1$ i.e. the vortex shedding mode, is the most dominant, stated that this mode is likely to be sensitive to the shape of the blunt body and to the nature of the separation of the flow from the body. Our results suggest that this is also the case for vortex shedding from non-axisymmetric bodies and is perhaps the case for all axisymmetric wakes in general. It would therefore appear that the main function of the multi-scale segments around the perimeter of the plates are to re-distribute the energy to a broader range of scales in the flow, as evident from the broader coherence spectra for the $D_f = 1.5$ plates in figure 11 compared to the disk in figure 9(a).

It is evident from the results that the geometrical properties of the plates have an influence on the vortex shedding energy, however it is feasible that these changes may affect other aspects of the wake also. One might expect that the clear decrease in vortex shedding energy may be related to or even cause a decrease in the size of the wake, for example. Figure 14 shows the relationship between the vortex shedding energy (Ξ) and the wake volume coefficient, defined as $C_V = \frac{2\pi}{\ell^3}\int_{5\ell}^{25\ell}\delta^2 dx$, where we see a clear correlation with the volume of the wake decreasing as the vortex shedding energy decreases. Cannon et al[11], who

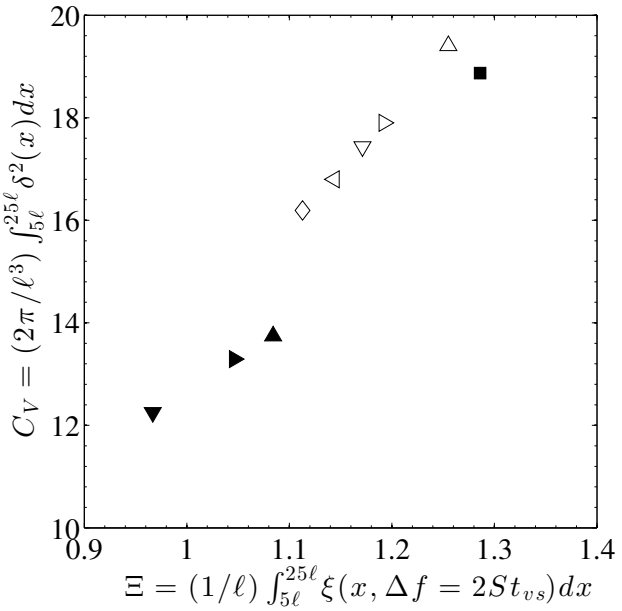

FIG. 14: Change in wake volume coefficient with energy of vortex shedding

used disks of varying porosity, observed a similar trend whereby increasing the porosity of the disk a smaller, yet broader, peak is observed at the vortex shedding frequency, along with the wake narrowing. This suggests that the vortex shedding structures are likely to be responsible for the size of the wake, but may not solely be responsible for the drag coefficient.

A theoretical framework has recently been presented[15] where by considering an energy balance of a bluff body moving through a stationary fluid (i.e. no free-stream turbulence is present), it was shown that the drag coefficient C_D is a function of the wake volume coefficient C_V and the average rate of turbulent kinetic energy dissipation in the **entire wake** i.e. $C_D = C_V C_{\bar{\varepsilon}}$. This simple relationship highlights that the large-scale structures, via the size of the wake, and the small-scale structures, via the average rate of turbulent kinetic energy dissipation, play an important role in determining the drag coefficient. In figure 15 we plot the drag coefficient of the $\ell = 128mm$ plates at a Reynolds number of $\approx 82,000$; the drag force was acquired using a ATI Nano17 force/torque sensor with a range of $35N$ in the drag force direction and a resolution of $6.25mN$. The sensor was mounted between the suspended aluminium mount and the plates, with data sampled for $60s$ at $100Hz$. Figure 15 qualitatively shows similar results to those shown in figure 5 of reference 15; as you increase the fractal iteration the drag coefficient increases up until a threshold value, after which there is a noticeable drop e.g. the $D_f = 1.33(5)$ plate in figure 15 and the

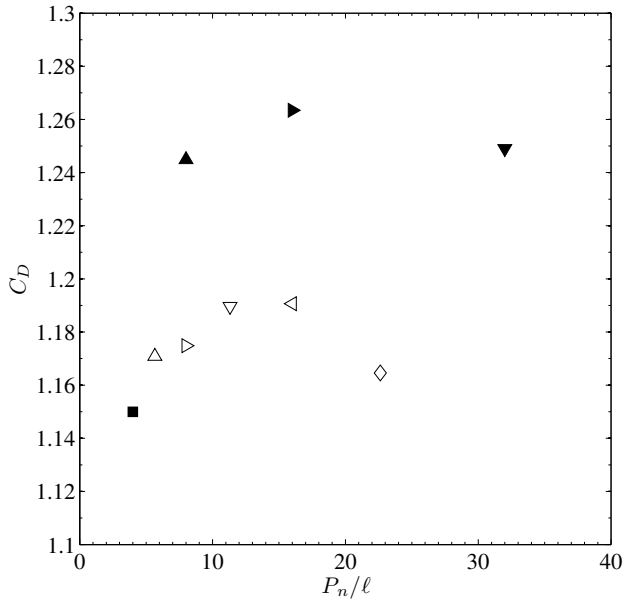

FIG. 15: Drag coefficient for the $\ell = 128mm$ plates

$D_f = 1.5(4)$ plate in figure 5 of reference 15. Therefore it would appear that by changing the physical boundary conditions of the wake generator (whilst keeping its frontal area constant), one is able to change the volume of the wake as well as the drag coefficient and therefore the average rate of kinetic energy dissipation. We believe that these fractal plates are essentially doing just that.

The multi-scale nature of these plates are reducing the energy of the large-scale structures, or conversely not injecting as much energy into these scales, but are injecting energy into a wide range of scales in the flow. In essence they are better mixers than the disk and square plate, generating higher levels of turbulence intensity in the wake for the same input velocity and plate area. This increase in turbulence intensity will result in an increase in the rate of turbulent kinetic energy dissipation, ε, hence the average rate of dissipation in the whole wake, $C_{\bar{\varepsilon}} = (\bar{\varepsilon}\ell)/U_\infty^3$, is larger. By diminishing the vortex shedding energy, the size of the wake will decrease (see figure 14), however this decrease is overwhelmed by the increase in $C_{\bar{\varepsilon}}$ (note however that C_V in figure 14 does not include data from 0 to 5ℓ and that this region also contributes both to C_V and $C_{\bar{\varepsilon}}$). It is therefore conceivable that as we introduce more length-scales along the perimeter of the plates i.e. increase the fractal dimension, $C_{\bar{\varepsilon}}$ will increase more than C_V decreases, hence we observe an initial increase in C_D (see figure 5 in[15]). As the length-scales on the perimeter become smaller, it is plausible that the decrease

in C_V becomes insurmountable by the increase in $C_{\bar{\varepsilon}}$, hence C_D would decrease for higher fractal iterations (see figure 5 in[15]). Understanding how this transition occurs would prove useful for flow manipulation purposes, and future studies will aim at directly investigating the dissipation in the wake, as well as the small scale features of the wake in general. Finally the behaviour of the dissipation in these wakes may also lead to a better understanding of the non-equilibrium region that has been observed in some of these wakes[16], highlighting another clear geometrical influence on turbulent axisymmetric wakes.

VI. CONCLUSION

Through an extensive set of hot-wire measurements, covering a large spatial domain downstream of the plates, we confirm recent findings of an apparent universal Strouhal number for the vortex shedding if the characteristic length of the plate is used as a normalising parameter. This Strouhal number is found to be $St = 0.11 \pm 0.005$. We also obtain a more robust measure for the vortex shedding energy, by integrating the energy spectra of the streamwise and radial velocity components and find that as fractal dimension and iteration increase, the vortex shedding energy decreases. Compared to a square plate, the vortex shedding energy for the $D_f = 1.5(3)$ plate over a given spatial domain is decreased by 60% for $\Delta f = 0$ to 25% for $\Delta f = 2St$. It is also found that although the vortex shedding energy is lower for the fractal plates compared to a disk and square plate initially, it takes longer for this energy to decay for the fractal plates.

The large-scale structures in the wake of these non-axisymmetric bodies were further investigated by considering two-point measurements. Remarkably, even though we change the physical boundary conditions and create plates with a complex and irregular shape, the wake was still able to arrange itself into a similar fashion to what is observed in the wake of a disk. The large-scale structures associated with the vortex shedding are shown to be associated with the first azimuthal mode for all the plates, but the amount of fluctuating energy within this mode decreases with increasing dimension and iteration, with the amount being 73% for the disk and 55% for the $D_f = 1.5(3)$ plate. Although this may lead one to conclude that these structures are created and exist in the wake regardless of the physical boundary conditions, it has been argued that they are responsible for how the energy is distributed to all the structures in the flow, which in turn may have consequences on the

drag coefficient, the size of the wake and the physical extent of the non-equilibrium region in some of these wakes[16].

ACKNOWLEDGEMENTS

We gratefully acknowledge the financial support received from EPSRC and from the EU FP7 Consortium on Optimisation for low Environment Noise impact AIRcraft (OPENAIR). We are also grateful for the support of the technicians from the Department of Aeronautics workshop for the help with the experiments. We also thank the reviewers for their constructive comments which helped improve the final version of this paper.

REFERENCES

[1]P. Holmes, JL L. Lumley, and G. Berkooz. *Turbulence, coherent structures, dynamical systems and symmetry*. Cambridge University Press, 1996.

[2]Heinrich E. Fiedler. Control of free turbulent shear flows. In *Flow Control*, pages 335–429. Springer, 1998.

[3]Jimmy Philip and Ivan Marusic. Large-scale eddies and their role in entrainment in turbulent jets and wakes. *Physics of Fluids*, 24(5):055108, 2012.

[4]Haecheon Choi, Woo-Pyung . P. Jeon, and Jinsung Kim. Control of flow over a bluff body. *Annual Review of Fluid Mechanics*, 40(1):113–139, 1 2008.

[5]Peter B. V. Johansson and William K. George. The far downstream evolution of the high-reynolds-number axisymmetric wake behind a disk. part 2. slice proper orthogonal decomposition. *Journal of Fluid Mechanics*, 555:387, 5 2006.

[6]J. B. Roberts. Coherence measurements in an axisymmetric wake(behind blunt body via signal analysis). *AIAA Journal*, 11:1569–1571, 1973.

[7]H. V. Fuchs, E. Mercker, and U. Michel. Large-scale coherent structures in the wake of axisymmetric bodies. *Journal of Fluid Mechanics*, 93(01):185–207, 1979.

[8]E. Berger, D. Scholz, and M. Schumm. Coherent vortex structures in thewake of a sphere and a circular disk at rest and under forced vibrations. *Journal of Fluids and Structures*, 4(3):231–257, 1990.

[9]S. C. Cannon. *Large-scale structures and the spatial evolution of wakes behind axisymmetric bluff bodies.* PhD thesis, The University of Arizona, 1991.

[10]S. J. Lee and P. W. Bearman. An experimental investigation of the wake structure behind a disk. *Journal of fluids and structures*, 6(4):437–450, 1992.

[11]S. Cannon, F. Champagne, and A. Glezer. Observations of large-scale structures in wakes behind axisymmetric bodies. *Experiments in fluids*, 14(6):447–450, 1993.

[12]Peter B. V. Johansson, William K. George, and Scott H. Woodward. Proper orthogonal decomposition of an axisymmetric turbulent wake behind a disk. *Physics of Fluids*, 14(7):2508, 2002.

[13]P A. Monkewitz. A note on vortex shedding from axisymmetric bluff bodies. *Journal of Fluid Mechanics*, 192:561–575, 1988.

[14]H. Higuchi, RW W. Anderson, and J. Zhang. Three-dimensional wake formations behind a family of regular polygonal plates. *AIAA Journal*, 34(6):1138–1145, 6 1996.

[15]J. Nedić, B. Ganapathisubramani, and JC. Vassilicos. Drag and wake characteristics of flat plates perpendicular to the flow with fractal edge geometries. *Fluid Dynamics Research*, 45(6):061406, 12 2013.

[16]J. Nedić, JC. Vassilicos, and B. Ganapathisubramani. Axisymmetric turbulent wakes with new non-equilibrium similairty scalings. *Phys. Rev. Lett.*, 111(14):144503, 10 2013.

[17]Elad Rind and Ian P. Castro. On the effects of free-stream turbulence on axisymmetric disc wakes. *Experiments in Fluids*, 53(2):301–318, 8 2012.